Journal of Materials Research and Technology 32 (2024) 1342–1353

Contents lists available at ScienceDirect

Journal of Materials Research and Technology

journal homepage: www.elsevier.com/locate/jmrt

Different impact of recovery annealing and thermal pressure treatments on the microstructure and mechanical properties of rejuvenated $Cu_{64}Zr_{36}$ metallic glasses: A molecular dynamics study

Rongkang Liu [a,1], Jiaqing Wu [a,1], Ruoyu Hai [a], Hongtao Zhong [a], Peiyou Li [b], Peng Xue [c], Ming Jen Tan [d], Yuanzheng Yang [a], Xiaoling Fu [a,*]

[a] School of Materials and Energy, Guangdong University of Technology, Guangzhou, 510006, People's Republic of China
[b] School of Materials Science and Engineering, Shaanxi University of Technology, Hanzhong, 723001, People's Republic of China
[c] Department of Materials Science and Technology, Ji Hua Laboratory, Foshan, Guangdong, 528200, People's Republic of China
[d] Singapore Centre for 3D Printing, School of Mechanical and Aerospace Engineering, Nanyang Technological University, Singapore, 639798, Singapore

ARTICLE INFO

Keywords:
Molecular dynamic
Metallic glasses
Medium-range order
Icosahedra
Rejuvenation

ABSTRACT

The interpenetrating connection of icosahedra network (ICOIN) was termed as structural skeleton, which could quantify the strength and ductility of MGs. The impact of different rejuvenation methods on medium-range order (MRO) alterations was rarely studied. This work employed molecular dynamics simulations to examine the difference in MRO evolution of metallic glasses treated by recovery annealing and thermal-pressure treatment during uniaxial tension. All of the specimens obtain enhanced ductility due to improved potential energy. During tension, ICOI of all rejuvenated specimens exhibits an increased destruction rate and a decreased transformation rate. However, there are some converse characteristics in the specimens under different rejuvenation methods. The rejuvenated specimens treated by recovery annealing exhibit increased free volume and decreased ICOIN density. After thermal-pressure treatment, the rejuvenated specimens demonstrated decreased free volume and enhanced ICOIN density. During tension, the enhancement of icosahedral free volume in specimens treated by thermal pressure largely decreased the ICOIN density, thereby increasing the ductility. After tension, the rejuvenated specimens under high pressure have a significant reduction in ICOIN density compared to those under recovery annealing. The significance of this work is to accurately regulate the ICOIN density of rejuvenated specimens.

1. Introduction

Metallic glasses (MGs), result from rapidly quenching a molten metal to bypass crystallization. Characterized by long-range disorder and short-range order, MGs lack typical crystalline defects like dislocations and stacking faults. Noteworthy properties of MGs encompass remarkable strength, hardness, corrosion resistance, and an outstanding elastic limit [1,2].

In the early 21st century, Miracle et al. [3] considered the difference in atomic size of MGs and introduced the efficient cluster packing model, highlighting the dominance of icosahedral cluster structures in these glasses. In contrast to short-range order (SRO), medium-range order (MRO) more aptly represents the complex structure of MGs. SRO is usually represented by icosahedral clusters, while MRO refers to how these icosahedral clusters and other polyhedral units connect and arrange themselves over a medium-range scale [4,5]. MRO extends beyond the first few nearest neighbors and describes how these SRO units connect over a longer range. The neighboring icosahedra can be connected by sharing their vertex, edge, face or volume, thereby forming four different types of connections [6]. Hereafter, the MRO resulting from volume-sharing type of icosahedral connection [7] are referred to "interpenetrating connection of icosahedra (ICOI)" [4]. The local connectivity of icosahedron by Wu et al. [8,9] and the interpenetrating connection of icosahedra (ICOI) by Lee et al. [4] involve the bonding of central atoms in icosahedra. The bond number of ICOI denotes as N. ICOI with high-N means that the central atom of icosahedron bonds with

* Corresponding author.
E-mail address: fuxiaoling@gdut.edu.cn (X. Fu).
[1] These authors contributed equally.

https://doi.org/10.1016/j.jmrt.2024.07.178
Received 20 April 2024; Received in revised form 23 July 2024; Accepted 24 July 2024
Available online 25 July 2024

many others of icosahedra. N is observed to range from 0 to 8. The structure connected by ICOI is termed the interpenetrating connection of icosahedra network (ICOIN). Lee et al. [4] found that ICOI with high-N exhibited higher shear deformation resistance, but it hindered the formation of shear transformation zones (STZs) in the specimen. ICOI with high-N increased the degree of strain localization, leading to an increase in strength and a decrease in ductility.

Owing to the typical brittle fracture at room temperature, the poor ductility of most MGs limited their structural applications [10,11]. To enhance the room-temperature ductility of MGs, mechanical and heat treatments are utilized for the rejuvenation of MGs. Rejuvenation is a process that induces structural excitation in MGs, propelling them to higher energy states and augmenting their free volume. Mechanical rejuvenation methods encompass cold rolling, shot peening, high-pressure torsion and irradiation [12–16]. In experiments, Saida et al. [17] subjected the relaxed $Zr_{55}Al_{10}Ni_5Cu_{30}$ MG heating to 1000 K followed by rapid quenching, which rejuvenated the MG efficiently. The recovery annealing process of the MG recovered the relaxation enthalpy by about 50%. Wang et al. [18] demonstrated that high-pressure annealing treatment was an effective way to activate $La_{60}Ni_{15}Al_{25}$ MG into higher energy states. In addition, high-pressure annealing treatment increased the relaxation enthalpy and the elastic modulus of the MG. In molecular dynamics (MD) simulations, Wang et al. [19,20] explored the evolution of rejuvenation levels in CuZr MGs by manipulating the annealing temperature and cooling rate. They found that faster cooling rates and higher annealing temperatures could improve the rejuvenation level of the specimens. Amigo et al. [21,22] applied pressure to rejuvenate CuZr MGs. They found a sustained reduction in both bulk and shear modulus with the increasing rejuvenation pressure. The reduction in bulk and shear modulus transitioned the deformation mode of the specimens from local shear bands to homogeneous deformation, enhancing the ductility of the specimens.

Presently, most of the structural analyses on rejuvenated MGs concentrate on their short-range order. The correlation between the evolution of medium-range order and ductility of MGs is not yet clear. This work uses different rejuvenation methods to effectively manipulate the density of ICOIN in MGs. This enables a deeper insight into the impact of medium-range order on mechanical properties of rejuvenated MGs, which contributes to explaining the enhanced ductility of rejuvenated MGs observed in experiments.

2. Simulation details

In this work, MD simulations of $Cu_{64}Zr_{36}$ MGs were performed using an open-source software Large-scale Atomic/Molecular Massively Parallel Simulator (LAMMPS) [23]. The interatomic interaction was described by the embedded atom method (EAM) potential for CuZr binary alloy proposed by Mendelev et al. [24]. The glass transition temperature of $Cu_{64.5}Zr_{35.5}$ metallic glass for this potential is T_g = 770 K [24], agreeing reasonably well with experimental value of 737 K [25]. Therefore, glass transition temperature of $Cu_{64.5}Zr_{35.5}$ MGs calculated by Mendelev-2009 potential can provide a reasonable reference for $Cu_{64}Zr_{36}$ MGs in this work. Initially, a pure Cu crystalline model was constructed, measuring 23.92 nm (X) × 11.96 nm (Y) × 2.79 nm (Z) with 50,400 atoms. In the initial model, 18,144 Cu atoms were randomly substituted with Zr atoms to achieve a $Cu_{64}Zr_{36}$ alloy composition. The model was relaxed for 2 ns at 2000 K and zero external pressure, then rapidly quenched to 1 K at a cooling rate of 1×10^{12} K/s to obtain the as-cast metallic glass sample (denoted as A_0 in Fig. 1(a)). According to the kink of the temperature-volume curve in Fig. 1(b), the glass-transition temperature (T_g) of $Cu_{64}Zr_{36}$ MG was approximately 770 K.

A_0 is as-cast sample without any recovery annealing or thermal pressure treatment. The procedure for preparing rejuvenated MGs is recovery annealing as depicted in Fig. 1(c), similar to the method proposed by Wang et al. [20]. We prepared different samples (from aged to rejuvenated) by recovery annealing with various annealing temperatures. Jun et al. [26] chose $1.00T_g - 1.43T_g$ as annealing temperatures to

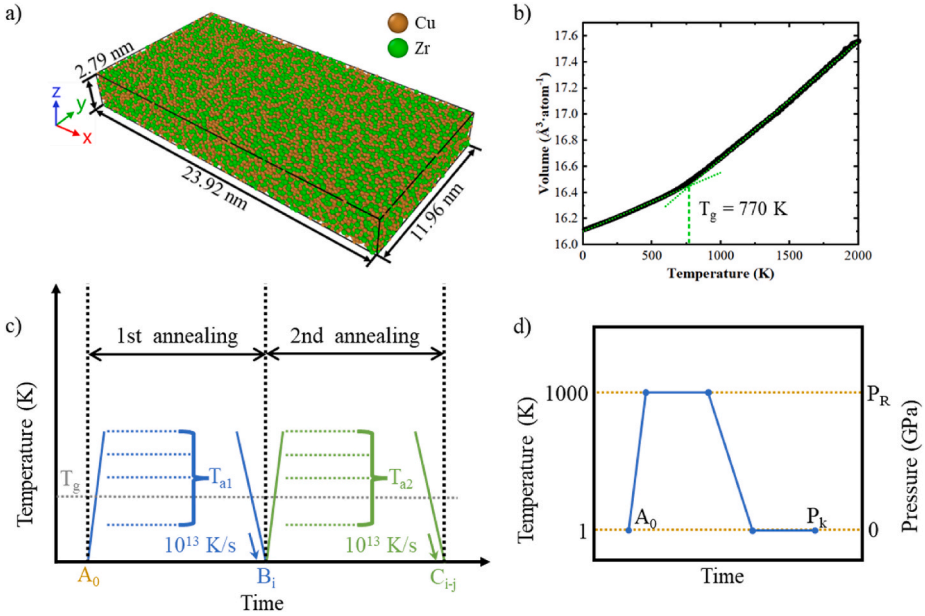

Fig. 1. a) The schematic diagram of as-cast $Cu_{64}Zr_{36}$ MG sample (denoted as A_0). b) Temperature-volume curve of A_0 during the cooling process. c) Schematic illustration of recovery annealing treatment process, the initial recovery annealing involves heating the A_0 specimen to the first annealing temperature (T_{a1}) between 600 K and 1200 K, maintaining this temperature for 1 ns, and then rapidly cooling to 1 K at a rate of 1×10^{13} K/s, resulting in one-time annealed MGs (B_i). In the second annealing process, B_i undergoes a second annealing at the second annealing temperature (T_{a2}) between 600 K and 1200 K, employing the same cooling rate to obtain the secondary annealed MGs (C_{i-j}). d) Schematic illustration of thermal pressure treatment process, A_0 is heated to 1000 K in 0.1 ns, with simultaneous application of rejuvenation pressure (P_R), P_R is a fixed value in the range of 0–70 GPa. Following a relaxation phase at 1000 K and the applied P_R for 2 ns, the specimens are quenched from 1000 K to 1 K at a cooling rate of 1×10^{12} K/s, with pressure reduction to 0 GPa. After relaxing for 4 ns at 1 K, the rejuvenated MGs (P_k) are obtained.

investigate the rejuvenation process of $Cu_{64}Zr_{36}$ metallic glass. Moreover, to show an aging to rejuvenation transition of Cu–Zr metallic glass, Wang et al. [19] chose the target annealing temperatures from 700 K (slightly lower than $T_g = 785$ K) to 1200 K. Referred from their work, we select 600 K − 1200 K ($T_g = 770$ K) as annealing temperatures to prepare the specimens from aging to rejuvenating. The first recovery annealing involved heating the A_0 specimen to the first annealing temperatures ($T_{a1} = 600$ K − 1200 K), and equilibrated at T_{a1} for 1 ns followed with a rapidly cooling process to 1 K with a cooling rate of 1×10^{13} K/s, resulting in one-time annealed MGs. One-time annealed MGs were denoted as B_i specimens; i × 100 represented the annealing temperature in the first annealing. In the second annealing process, B_i underwent a second annealing at the second annealing temperatures (T_{a2} = 600 K–1200 K) with a cooling rate of 1×10^{13} K/s to obtain the secondary annealed MGs. The secondary annealed MGs were denoted as $C_{i\text{-}j}$ specimens; i-j represented the secondary annealing of B_i at the temperature of j × 100. The annealing temperatures ($T_{a1}/T_{a2} = 600$ K − 1200 K) were chosen to observe the transition of the specimens from aging to rejuvenation. In this method, annealing temperatures were taken every 100 K for simulation (600 K, 700 K, 800 K, 900 K, 1000 K, 1100 K, 1200 K).

The procedure for preparing rejuvenated specimens via thermal pressure treatment is based on the approach by Amigo et al. [21], as depicted in Fig. 1(d). A_0 specimen was rapidly heated to 1000 K, approximately $1.3T_g$, within 0.1 ns, while applying rejuvenation pressures ($P_R = 0$ GPa −70 GPa). This was followed by a relaxation phase at 1000 K and the applied P_R for 2 ns, then a quenching process from 1000 K to 1 K at a cooling rate of 1×10^{12} K/s, with concurrent pressure reduction to 0 GPa. The process culminated in obtaining the rejuvenated specimens by relaxing them for 4 ns at 1 K under no external pressure. The rejuvenated specimens prepared by thermal pressure treatment were denoted as P_k specimens; k represented the rejuvenation pressure. For example, after the as-cast sample A_0 is treated by thermal-pressure treatment under a rejuvenation pressure of 10 GPa, P_{10} is obtained. Prior research indicated that annealing temperatures in the range of $1.1T_g$ − $1.3T_g$ facilitated MGs rejuvenation [5,27]. In this method, rejuvenation pressures were taken every 10 GPa for simulation (0 GPa, 10 GPa, 20 GPa, 30 GPa, 40 GPa, 50 GPa, 60 GPa, 70 GPa).

The model employed periodic boundary conditions (PBCs) within an NPT ensemble (constant number, pressure and temperature). Temperature and pressure regulation was achieved through the application of the Nosé-Hoover thermostat and Parrinello-Rahman techniques [28,29]. During the uniaxial tensile simulation, PBCs were preserved along the X and Z axes, while the Y axis was altered to a free surface configuration. The free surface facilitated shear offset on surface of the model, which was critical for initiating shear band formation [30,31].

The first step of statistical method used to analyze ICOI with different N is performing Voronoi Analysis in OVITO [32]. After this, the central atoms of <0,0,12,0> polyhedra are selected. Individual <0,0,12,0> polyhedra are linked with neighboring <0,0,12,0> polyhedra to form ICOI. Finally, the population of ICOI with different N can be evaluated. The specific steps and details of establishing ICOI in this work are shown in Supplementary Material Fig. S1. Fig. 2(a) illustrates the distribution of the icosahedra in A_0, highlighting only the atoms at the center of icosahedra. Fig. 2(b) demonstrates the local ICOIN, measuring 1.59 nm (X) × 1.71 nm (Y) × 1.44 nm (Z) with 35 atoms. The discontinuity with neighboring ICOIs prevents the ICOIN from forming a completely interconnected network in the specimen. The configurations of ICOIs with different N are shown in Fig. 2(c)–(d) and (e).

3. Results and discussion

3.1. Evolution of potential energy and free volume

Fig. 3(a) illustrates that the first annealing temperatures below 800 K, the average atomic potential energy of the specimens closes to or falls below the baseline level of A_0 specimen. Specifically, the second annealing temperature at 700 K ($C_{8\text{-}7}$), this potential energy reaches its minimum. Conversely, above 800 K, there is a marked increase in the average atomic potential energy of the specimens relative to A_0, signifying the rejuvenation of the specimens. The increasing trend gradually decelerates beyond 1000 K, indicating that the rejuvenation is approaching saturation.

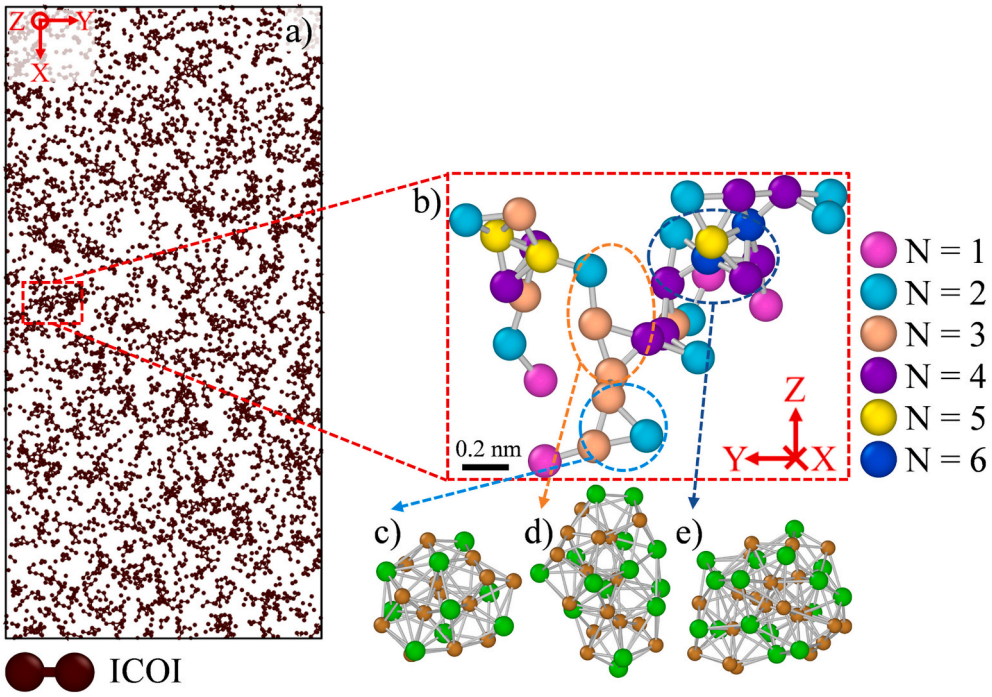

Fig. 2. a) The snapshot showing the distribution of ICOIN in A_0. b) Example of the local ICOIN: a chain-like patch consisting of 35 icosahedra with different N. Only the center atoms of the icosahedra are plotted as points. Typical configurations of ICOIs with different bond numbers of c) N = 2, d) N = 3, and e) N = 6. The brown (small) and green (large) spheres indicate Cu and Zr atoms, respectively.

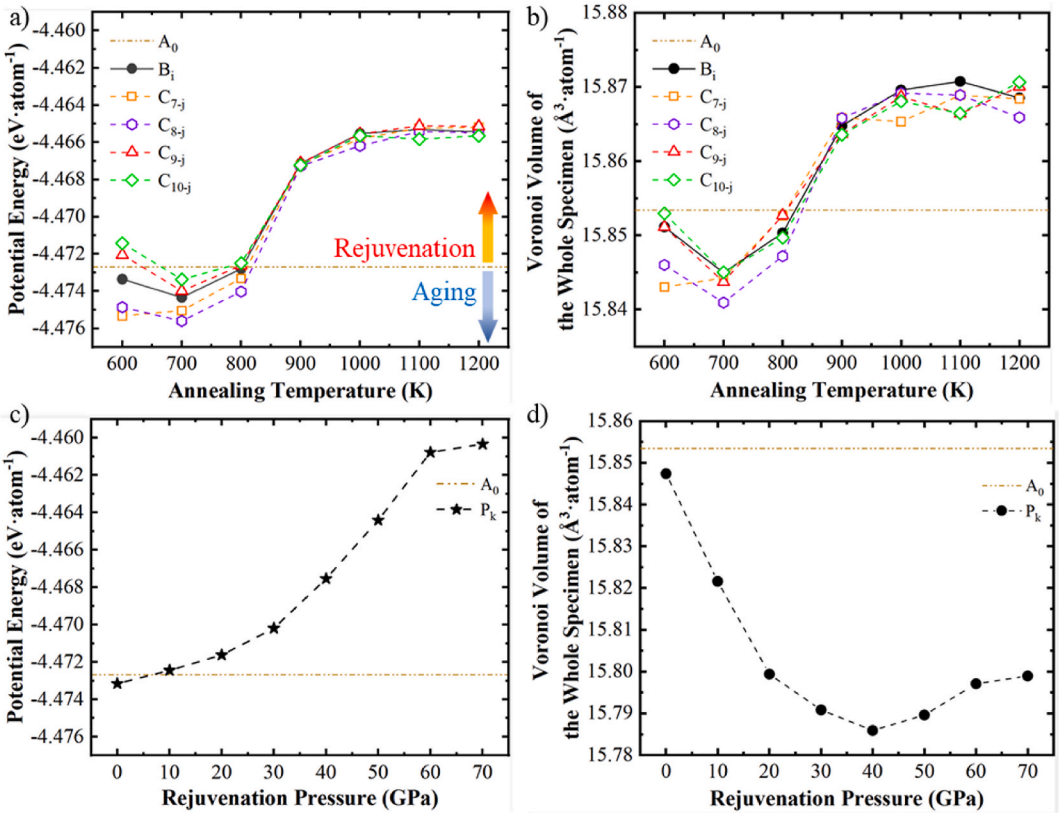

Fig. 3. a) The average atomic potential energy and b) the average Voronoi volume of the whole specimen under recovery annealing treatment. One-time annealed MGs are denoted as B_i specimens; i × 100 represents the annealing temperature in the first annealing. The secondary annealed MGs are denoted as $C_{i\text{-}j}$ specimens; i-j represents the secondary annealing of B_i at the temperature of j × 100. c) The average atomic potential energy and d) the average Voronoi volume of the whole specimen under thermal pressure treatment. The rejuvenated specimens prepared by thermal pressure treatment are denoted as P_k specimens; k represents the rejuvenation pressure. The horizontal dotted line is the average atomic potential energy and average Voronoi volume of A_0.

For the specimens under secondary annealing, a notable decrease in potential energy is observed below 800 K, reaching its nadir in $C_{8\text{-}7}$. When the annealing temperature is above 1000 K, MGs exhibit no substantial rise in potential energy. Therefore, in subsequent work, more attention will be paid to specimens with annealing temperatures between 700 K and 1000 K. This aligns with Wang et al. [20], indicating a saturation point in potential energy enhancement through repeated recovery annealing at high temperatures. As the atomic core volume generally remains constant, the change in the Voronoi volume directly reflects the variation in free volume [33]. The schematic diagram of Voronoi volume, free volume and atomic core volume is shown in Supplementary Material Fig. S2. As depicted in Fig. 3(b), the Voronoi volume in the specimens under recovery annealing directly correlates with atomic potential energy. An increase in Voronoi volume can be observed in the rejuvenated specimens, whose latest annealing temperature is higher than 800 K. A decrease in Voronoi volume can be observed in the aged specimens, whose latest annealing temperature is lower than 800 K.

Fig. 3(c) shows that the specimens under thermal pressure treatment transform into a rejuvenated state, characterized by a gradual increase in potential energy until saturation. In Fig. 3(d), as the P_R increases, the Voronoi volume of the specimens under thermal-pressure treatment is consistently lower than A_0, corroborating the findings of Amigo et al. [22]. Moreover, the change of Voronoi volume is negative, with a minimum value corresponding to 40 GPa case and then a positive slope happens. All in all, the rejuvenation pressure brings the samples to higher energy states. These results are in line with the report of Wang et al. [34].

3.2. Evolution of SRO

Voronoi polyhedral cluster is defined as a polyhedron of the minimum volume containing the atom, which consists of the perpendicular bisectors of the lines connecting that atom to its neighboring atoms [35]. Voronoi polyhedral cluster is characterized by the Voronoi index $< n_3, n_4, n_5, n_6 >$, where n_v denotes the number of v-edge faces [36]. The clusters including <0,0,12,0>, <0,2,8,2>, and <0,1,10,2> possess higher degree of five-fold local symmetry [37]. In contrast, clusters including <0,2,6,4> and <0,3,6,4> exhibit lower degree of local five-fold symmetry. In Fig. 4(a), as the annealing temperature increases ($B_7 \rightarrow B_9 \rightarrow B_{10}$), <0,0,12,0> exhibits significant decrease. The aged specimens B_7 and $C_{8\text{-}7}$ contain a notably higher quantity of full icosahedra compared to the rejuvenated specimens B_9, B_{10} and $C_{10\text{-}10}$. To be noted, the fractions of <0,0,12,0> in B_9, B_{10} and $C_{10\text{-}10}$ samples are 7.375%, 7.335% and 6.899% respectively, which are lower than in the A_0 (as-cast) case (8.560%) as shown in Fig. 4(a). From B_9, B_{10} to $C_{10\text{-}10}$, the atomic structure becomes less packed. In Fig. 3(b), the atomic volume of rejuvenated B_9, B_{10} and $C_{10\text{-}10}$ samples are 15.865 $Å^3 \cdot atom^{-1}$, 15.870 $Å^3 \cdot atom^{-1}$, and 15.868 $Å^3 \cdot atom^{-1}$ respectively. These values are higher than that of the A_0 case, which is 15.853 $Å^3 \cdot atom^{-1}$. This variation reveals that the relative atomic packing efficiency follows the order: $A_0 > B_9 > C_{10\text{-}10} > B_{10}$. Nevertheless, there seems to be a contradiction in B_{10}, which has more <0,0,12,0> but a less dense state compared to $C_{10\text{-}10}$. This matter may refer to other lower local five-fold symmetry Voronoi polyhedrons <0,2,6,4> and <0,3,6,4>. In Fig. 4(a), the fractions of <0,2,6,4> and <0,3,6,4> in B_{10} (6.216%) is higher than $C_{10\text{-}10}$ (6.145%), indicating B_{10} may have less-packed atomic structure.

As observed in Fig. 4(b), when the specimens under thermal-pressure treatment, higher five-fold local symmetry clusters have an incremental

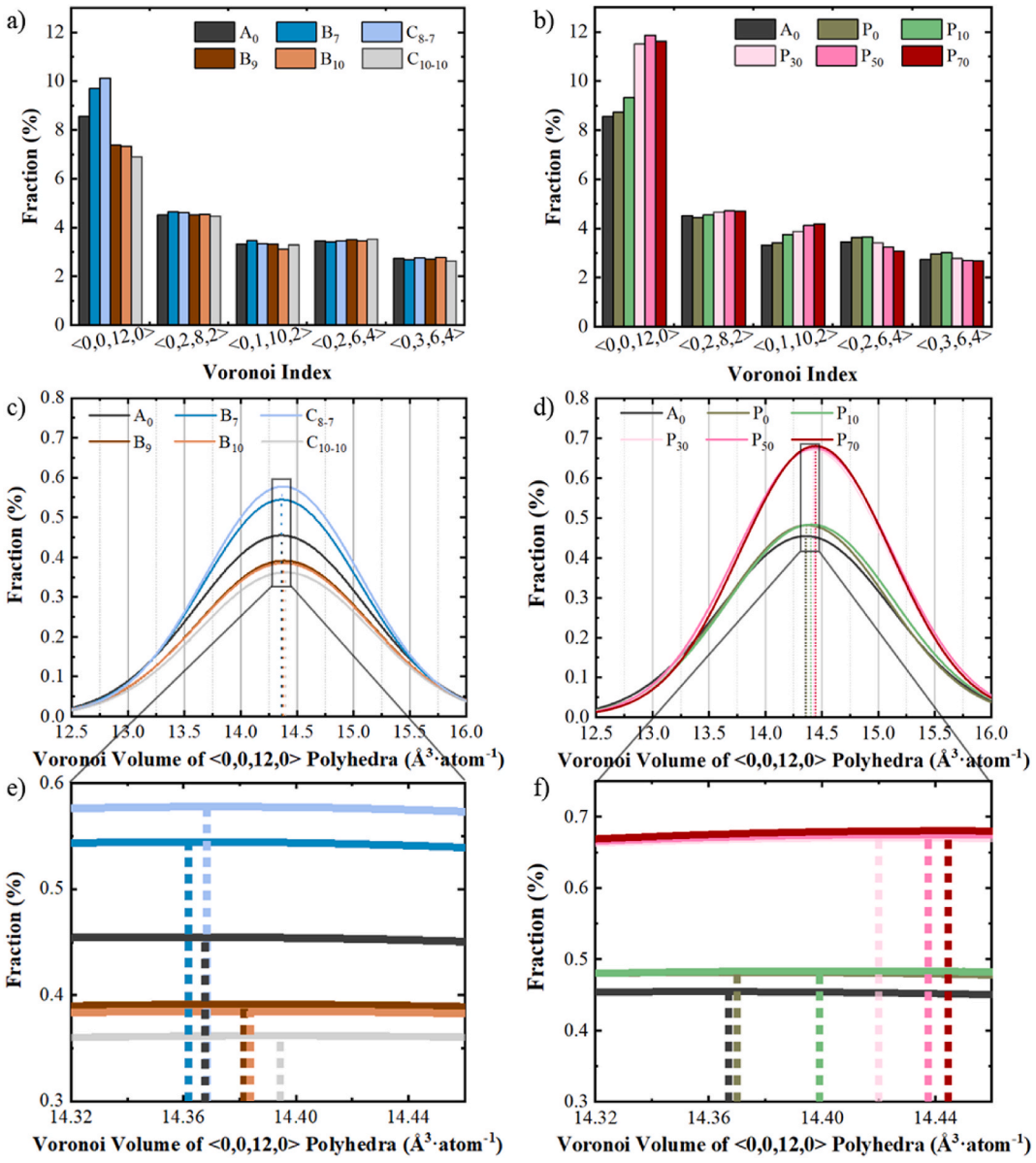

Fig. 4. The fraction of Voronoi polyhedrons in the specimens under a) recovery annealing treatment and b) thermal pressure treatment; Gaussian distribution of the Voronoi volume of <0,0,12,0> polyhedra in the specimens under c) recovery annealing treatment and d) thermal pressure treatment; e) and f) are magnified images of Fig. 4(c) and (d) respectively, used to observe the evolution of the peak position. The fraction is the ratio of the number of icosahedra to the total number of atoms in the specimen.

increase with rising treatment pressure P_R. In contrast, lower five-fold local symmetry clusters show a consistent decline with the increasing treatment pressure P_R. All samples present positive changes in potential energy as the pressure increases. To be noted, a decrease in the Voronoi volume of the whole specimen is distinguished in the $0 - 40$ GPa range, with no further decrease occurring above 40 GPa (Fig. 3(d)), similar to the work of Amigo [21,38], Miyazaki [39] and Wang [34]. Moreover, Miyazaki et al. [39] and Wang et al. [34] both reported that increasing pressure enhances the fraction of <0,0,12,0> to a certain limit of 30 GPa, after which it decreases with further increasing pressure. The effect of thermal pressure treatment on fraction of <0,0,12,0> in this work is shown in Supplementary Material Fig. S3. Similarly, the fraction of <0, 0,12,0> decreases when pressures exceeds 40 GPa (Fig. S3), corresponding to an increase in Voronoi volume (Fig. 3(d)). Therefore, the MGs with high Voronoi volume have more densely packed structure due to enhanced icosahedral order (<0, 0, 12, 0>) under the effect of pressure.

Since not all the <0,0,12,0> have the same Voronoi volume, the Gaussian curves of the Voronoi volume of <0,0,12,0> in the specimens under recovery annealing treatment and thermal pressure treatment are shown in Fig. 4(c) and (d). The Voronoi volume of <0,0,12,0> here corresponds to the Voronoi volume calculated for the center atom of each <0,0,12,0>. The peak positions along horizontal axis in Fig. 4 (c) and 4(d) represent the Voronoi volume size of <0,0,12,0> that appears most frequently in the specimens, and the peak values along vertical axis in Fig. 4 (c) and 4(d) indicate the fraction of <0,0,12,0> that have the Voronoi volume size corresponding to the peak position. For example, the peak position and the peak values of A_0 are 14.355 $Å^3 \cdot atom^{-1}$ and 0.455%, respectively. The <0,0,12,0> Voronoi volume with 14.355 $Å^3 \cdot atom^{-1}$ appears most frequently in the A_0 as-cast specimens. Fig. 4(e) shows that the peak positions of B_7 and C_{8-7} were akin to A_0. Compared to A_0, there is a rightward shift in the peak position of B_9 and B_{10}, indicating Voronoi volume of <0,0,12,0> that appears most becomes larger [19]. Under thermal-pressure treatment, the peak values are

continuously increasing as shown in Fig. 4(d), indicating the fraction of <0,0,12,0> that have the Voronoi volume size corresponding to the peak position increases. In the specimens under thermal-pressure treatment, the rightward shift in peak position is more pronounced with increasing P_R compared to the specimens under recovery annealing, as shown in Fig. 4(f). When the P_R reaches 70 GPa, the peak position is about 14.450 $Å^3$·$atom^{-1}$. Compared to A_0, Voronoi volume of <0,0,12,0> that appears most frequently increases with increasing P_R. The larger Voronoi volume of the maximum frequency <0,0,12,0> may contribute to an increase in Voronoi volume of the whole sample, but it cannot solely determine the Voronoi volume of the whole sample. During preparation, an increase in pressure results in the compression of the specimens, leading to a reduction in size of the specimens. This induces significant deformation among sparsely arranged atomic clusters, promoting the formation of icosahedra. An increased count of icosahedra leads to a reduction in the average Voronoi volume. Throughout the decompression and cooling phases, the quantity of icosahedra does not exhibit any significant alterations. However, the recovery of the specimens' size increases the icosahedral free volume.

3.3. Evolution of mechanical property and MRO during tension

The stress-strain curve in Fig. 5(a) indicates that the strength of the specimens is closely associated with their aging and rejuvenation levels. B_7 and $C_{8\text{-}7}$ show a little higher strength than A_0. B_{10} and $C_{10\text{-}10}$ show similar rejuvenation levels and demonstrate comparably lower strength than B_7, $C_{8\text{-}7}$ and A_0. Fig. 5(b) demonstrates that an increase in P_R is associated with a corresponding decrease in the strength of the specimens.

In the studies conducted by Wu et al. [9] and Yang et al. [40], the average value <N> served as a representation of the level of N. The calculation formula of <N> is $\langle N\rangle = \Sigma NF(N)$. Among the formula, N is the bond number of ICOI, and $F(N)$ is the percentage of ICOI with this N to the total number of ICOI. <N> is a good indicator to show the degree of ICOI. The increase or decrease of <N> values indicates the aggregation or disruption of the ICOI.

Miyazaki et al. [41,42] found that thermal rejuvenation is realized only when annealing temperatures T_a was above $1.1T_g$ and the cooling rate after isothermal annealing (1×10^{13} K/s) was higher than that of the initial melt-quenching process (1×10^{12} K/s). They reported that rejuvenation decreases the fraction of <0,0,12,0> and the degree of local clustering among icosahedra. Inversely, when annealing temperatures T_a was below 1.1 T_g, aging shows opposite phenomena. In this work, aging (B_7 and $C_{8\text{-}7}$) increases the fraction of <0,0,12,0> and the degree of ICOI before loading (Figs. 4(a) and 5(c)), corresponding well with Miyazaki's work [41,42]. Specifically, when $\varepsilon = 0$, the <N> value of $C_{8\text{-}7}$ is the largest, exceeding the <N> value of as-cast specimen A_0. It is worth noting that the aging specimen $C_{8\text{-}7}$ has the minimum value of potential energy in Fig. 3(a). As mentioned above, the minimum energy specimen $C_{8\text{-}7}$ shows the highest fraction of <0,0,12,0> (Fig. 4(a)) and the highest degree of ICOI at $\varepsilon = 0$ (Fig. 5(c)).

In Fig. 5(d), as P_R increases, both the rejuvenation level and <N> of the specimens under thermal-pressure treatment continue to increase at $\varepsilon = 0$. Once the values of P_R surpass 30 GPa, <N> tends towards saturation. In the tensile test, aged specimens shown in Fig. 5(c) demonstrate a more significant reduction in <N>. Furthermore, the reduction in <N> for rejuvenated specimens slows down. Conversely, during the tensile test depicted in Fig. 5(d), the specimens with higher <N> undergo a more marked reduction, suggesting a more severe disruption of ICOIN.

As depicted in Fig. 6(a), to further analyze the ductility of the specimens, this study quantify the failure strain rate (β) during the stress

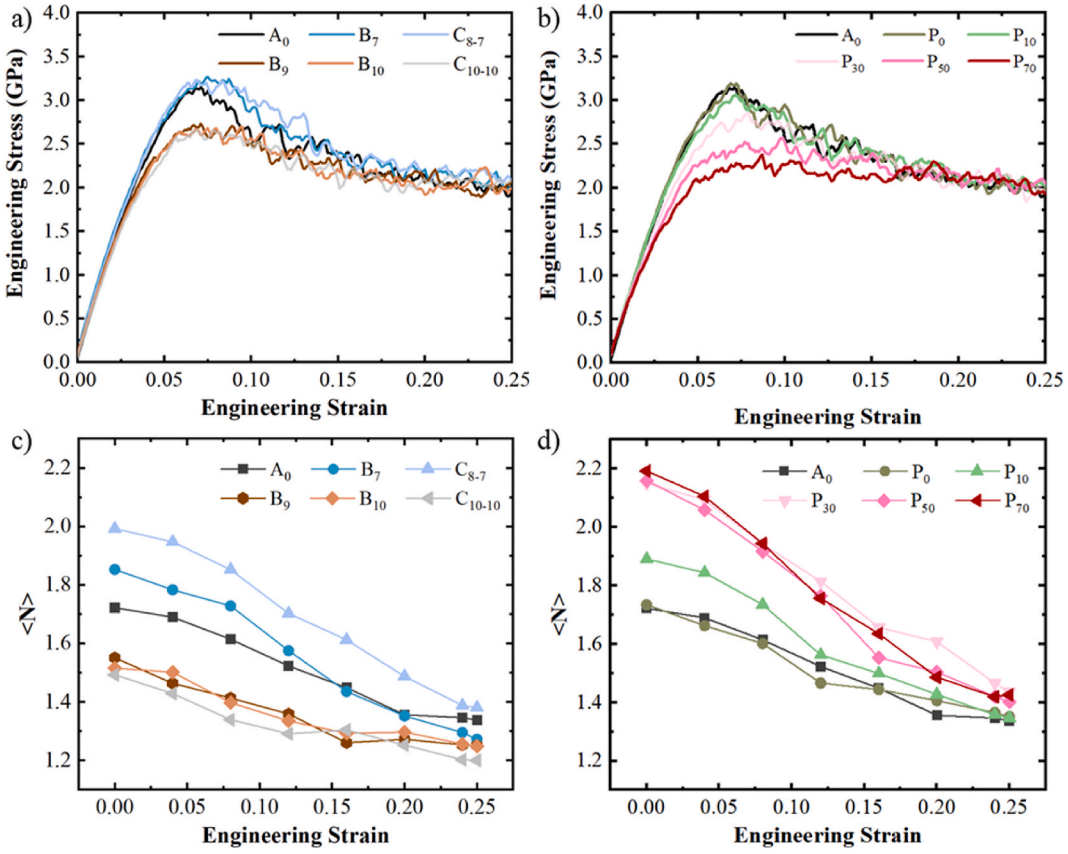

Fig. 5. Stress-strain curve of the specimens under a) recovery annealing treatment and b) thermal-pressure treatment; Evolution of <N> during the tension process of the specimens under c) recovery annealing treatment and d) thermal pressure treatment.

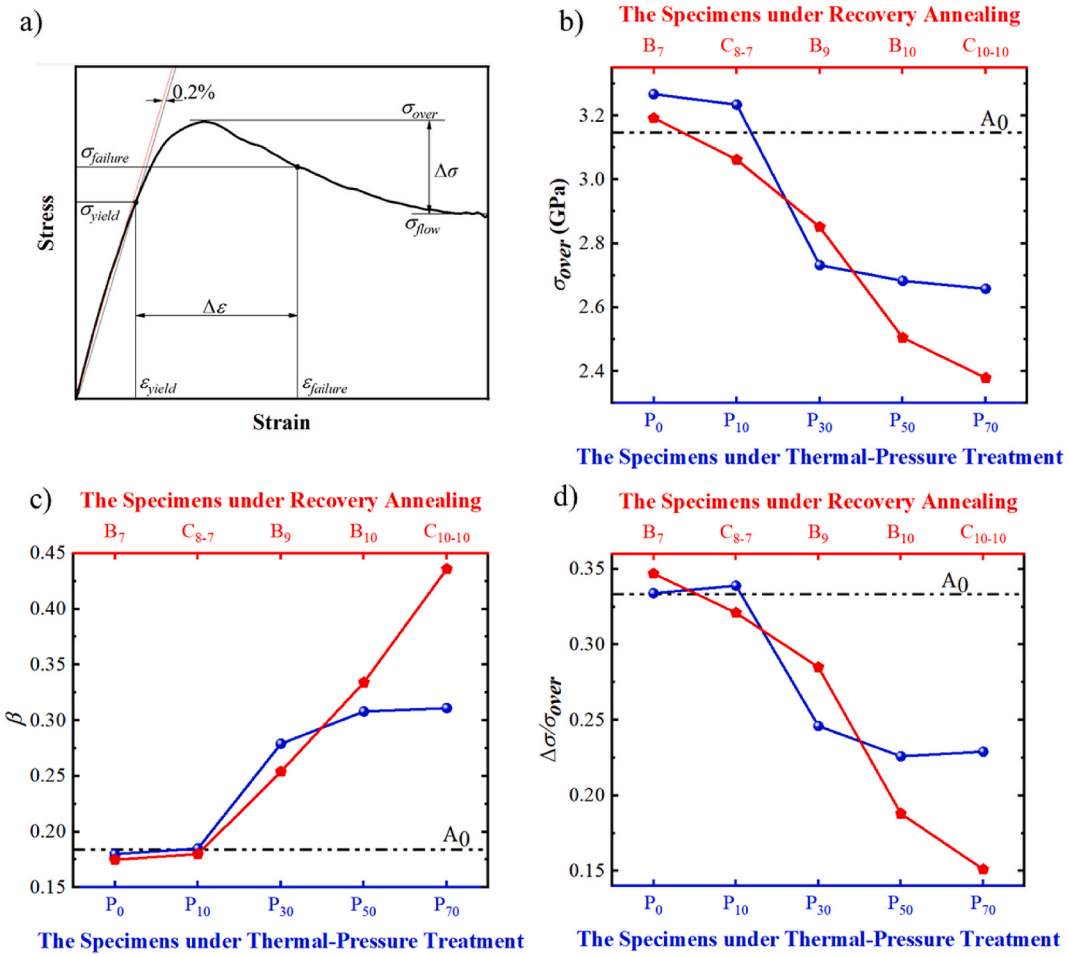

Fig. 6. (a) Schematic diagram of stress-strain curves for various stress and strain definitions used to characterize ductility. (b) σ_{over}, (c) β and (d) $\Delta\sigma/\sigma_{over}$ of the specimens under recovery annealing heat treatment and thermal-pressure treatment.

relaxation phase [43]. The formula for β is defined as: $\beta = \Delta\varepsilon \Big/ \left(\frac{\Delta\sigma}{\sigma_{failure}}\right)$, where $\Delta\sigma$, the stress difference, is calculated as $\Delta\sigma = \sigma_{over} - \sigma_{flow}$. Here, σ_{over} denotes the peak stress, and σ_{flow} represents the flow stress. The strain difference ($\Delta\varepsilon$) is calculated using the formula $\Delta\varepsilon = \varepsilon_{failure} - \varepsilon_{yield}$, where $\varepsilon_{failure}$, the failure strain. The failure stress ($\sigma_{failure}$) is computed using the formula $\sigma_{failure} = \frac{\sigma_{over}+\sigma_{flow}}{2}$. To get the yield stress (σ_{yield}) and the yield strain (ε_{yield}), Guo et al. [44] plotted a line parallel to the elastic region of the stress-strain curve from the origin and displaced the line rightward by 0.2%. From the interception between the shifted line and the stress-strain curve, the σ_{yield} and ε_{yield} were obtained. A higher β value signifies the enhanced ductility in the specimens. Furthermore, the degree of strain localization in the specimens is quantified by the normalized stress difference ($\Delta\sigma/\sigma_{over}$) [45,46]. A reduced $\Delta\sigma/\sigma_{over}$ value signifies the degree of strain localization decreasing in the specimens, indicative of a more homogenous deformation pattern. σ_{over}, β and $\Delta\sigma/\sigma_{over}$ of the specimens under recovery annealing heat treatment and thermal-pressure treatment are shown in Fig. 6(b)–(d).

Table 1 presents a summary of the stress and strain data for the specimens. The β values and $\Delta\sigma/\sigma_{over}$ values for the aged specimens B_7 and C_{8-7} closely align with those of A_0, suggesting analogous deformation behaviors. As the annealing temperature increases, there is a

Table 1
The peak stress (σ_{over}), the flow stress (σ_{flow}), the stress difference between peak stress and flow stress ($\Delta\sigma$), the strain difference between yield strain and failure strain ($\Delta\varepsilon$), the failure strain rate during the stress relaxation phase (β), and the normalized stress difference ($\Delta\sigma/\sigma_{over}$) of the specimens under recovery annealing treatment and thermal pressure treatment.

Rejuvenated method	Specimen	σ_{over} (GPa)	σ_{flow} (GPa)	$\Delta\sigma$ (GPa)	$\Delta\varepsilon$	β	$\Delta\sigma/\sigma_{over}$
–	A_0	3.146	2.099	1.047	0.073	0.184	0.333
Recovery annealing treatment	B_7	3.267	2.175	1.092	0.072	0.180	0.334
	C_{8-7}	3.234	2.137	1.097	0.075	0.185	0.339
	B_9	2.732	2.061	0.671	0.078	0.279	0.246
	B_{10}	2.683	2.077	0.606	0.078	0.308	0.226
	C_{10-10}	2.658	2.050	0.608	0.080	0.311	0.229
Thermal-pressure treatment	P_0	3.192	2.085	1.107	0.069	0.175	0.347
	P_{10}	3.062	2.080	0.982	0.084	0.180	0.321
	P_{30}	2.851	2.040	0.812	0.067	0.254	0.285
	P_{50}	2.505	2.034	0.471	0.071	0.334	0.188
	P_{70}	2.379	2.020	0.358	0.074	0.436	0.151

consistent rise in the β values for the rejuvenated specimens B_9, B_{10} and $C_{10\text{-}10}$, accompanied by a gradual decrease in $\Delta\sigma/\sigma_{over}$ values. The β and $\Delta\sigma/\sigma_{over}$ values for P_0 specimen and P_{10} specimen are close to those of A_0. However, with the progressive increase in P_R, there is a significant increase in β values, alongside a continuous reduction in $\Delta\sigma/\sigma_{over}$ values. This suggests that the specimens demonstrate decreased strain localization and enhanced ductility upon entering the rejuvenated state. The similar β values and $\Delta\sigma/\sigma_{over}$ values for B_{10} and $C_{10\text{-}10}$ in Table 1 suggest a similar level of ductility. This supports the idea that the degree of rejuvenation was saturated at high temperatures, as depicted in Fig. 3 (a).

The Von Mises stress (σ_{Mises}) serves as a measure for the elastic fluctuations in MGs, predicting atomic strain alterations during the elastic phase and acting as an indicator of subsequent shear band behavior in MGs [47,48]. Under tensile loading, these high σ_{Mises} regions are prone to initiate localized deformation, culminating in STZ formation [47,49]. Fig. 7 illustrates the distribution of ICOIN and σ_{Mises} in MGs before tension. In the figure, pink circles denote regions of high-density ICOIN coupled with low σ_{Mises}, whereas purple circles represent areas with low-density ICOIN and increased σ_{Mises}. ICOIN is commonly considered the structural backbone within MGs [50,51]. A higher value of <N> correlates with a denser ICOIN formation. Fig. 7(b) revealed that under recovery annealing, the specimens with a higher degree of rejuvenation have a lower value of <N>. In comparing A_0 with B_7, the density of ICOIN in aged specimens increases while σ_{Mises} decreases. Conversely, for B_{10}, the ICOIN becomes noticeably sparser, accompanied by an increase in areas of high σ_{Mises}. This suggests that subjected to recovery annealing, rejuvenated specimens exhibit a reduction in the value of <N>, leading to a lower ICOIN density. Consequently, this sparser atomic arrangement within the specimens leads to increased potential nucleation sites for STZs, ultimately enhancing ductility.

Fig. 7(c) shows that under thermal-pressure treatment, there is an increase in <N> values for MGs correlating with the rise in P_R. However, in the case of P_{70} specimen, despite the increased density of ICOIN, there is a concurrent elevation in σ_{Mises}. This observation aligns with the findings in Fig. 4(d), which indicates an increase in the free volume of icosahedral clusters with rising P_R. An increase in the icosahedral free volume signifies an increased distance between adjacent icosahedra, consequently diminishing the stability of the ICOIN. This ultimately leads to an increase in σ_{Mises} of the specimens under high pressure.

Fig. 8 displays the tensile stress-strain curves alongside the percentage of N for MGs. Lee et al. [4] employed the percentage change in N during deformation as a metric to elucidate deformation behavior of MGs. Fig. 8 illustrates that, after the tensile processing, there is a notable decline in the frequency of $N \geq 2$, concomitant with a continuous increase in the occurrence of $N = 0$ and $N = 1$. Fig. 8(b) shows that in B_7, the proportion of $N \geq 4$ after deformation decreases to approximately 40%, whereas the fraction of $N = 0$ escalates to more than 200% of its initial value. Conversely, rejuvenated specimens like B_9 and B_{10} preserve about 60% of $N \geq 4$ after deformation, but the proportion of $N = 0$ rises to just over 120% of its original value.

Fig. 8 (c) demonstrates that under thermal pressure treatment, P_0 specimen displays a change in N post-deformation akin to A_0. After deformation, the proportion of $N \geq 4$ declines to approximately 40%, and the percentage of $N = 0$ surges to over 160% of its initial value. However, with an ongoing increase in P_R, P_{30} specimen and P_{70} specimen show a marked shift in the trend of N's change following tensile deformation. The proportion of $N \geq 4$ steadily decreases after deformation, stabilizing at about 30%, whereas the percentage of $N = 0$ escalates to more than 240% of its original value. Fig. 8 indicates that these two different methods result in almost inverse alterations in N during tension of rejuvenated specimens.

Integrating the atomic shear strain under tension in Fig. 9 with the percentage change in N from Fig. 8 allows for further elucidation of the deformation behavior exhibited by MGs. In Fig. 9(b), under recovery annealing, aged specimens persistently disrupt the internal atomic structures characterized by high-N during the extension of shear bands. Ultimately, it results in a deformation pattern characterized by the formation of a primary shear band traversing the entire specimen. Rejuvenated specimens initiate STZs within regions marked by low-density ICOIN and sparsely arranged atoms. The growth of these STZs is unable to penetrate dense ICOIN regions, resulting in the disruption of only a restricted fraction of high-N structures.

In Fig. 9(c), the shear band behavior during tension in P_0 specimen

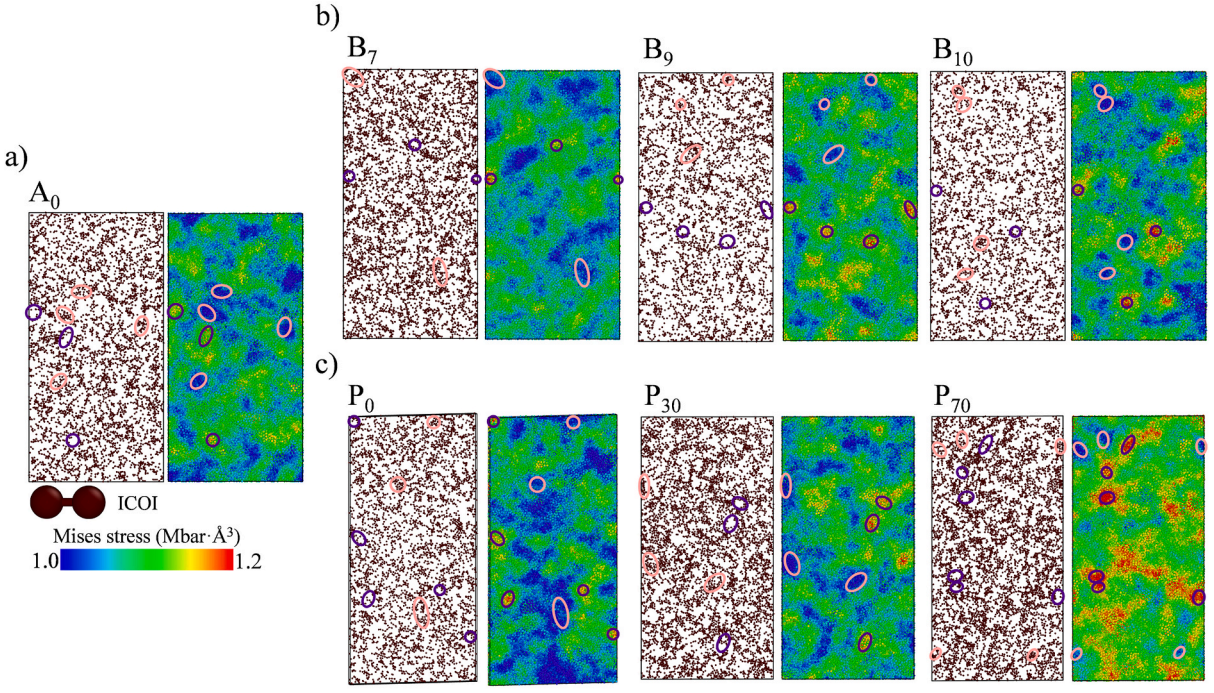

Fig. 7. ICOIN and σ_{Mises} distribution diagram of a) A_0, the specimens under b) recovery annealing treatment and c) thermal pressure treatment before tension. Local high densities of ICOIN correlates lower σ_{Mises} (pink circles), and local low densities of ICOIN correlates higher σ_{Mises} (purple circles).

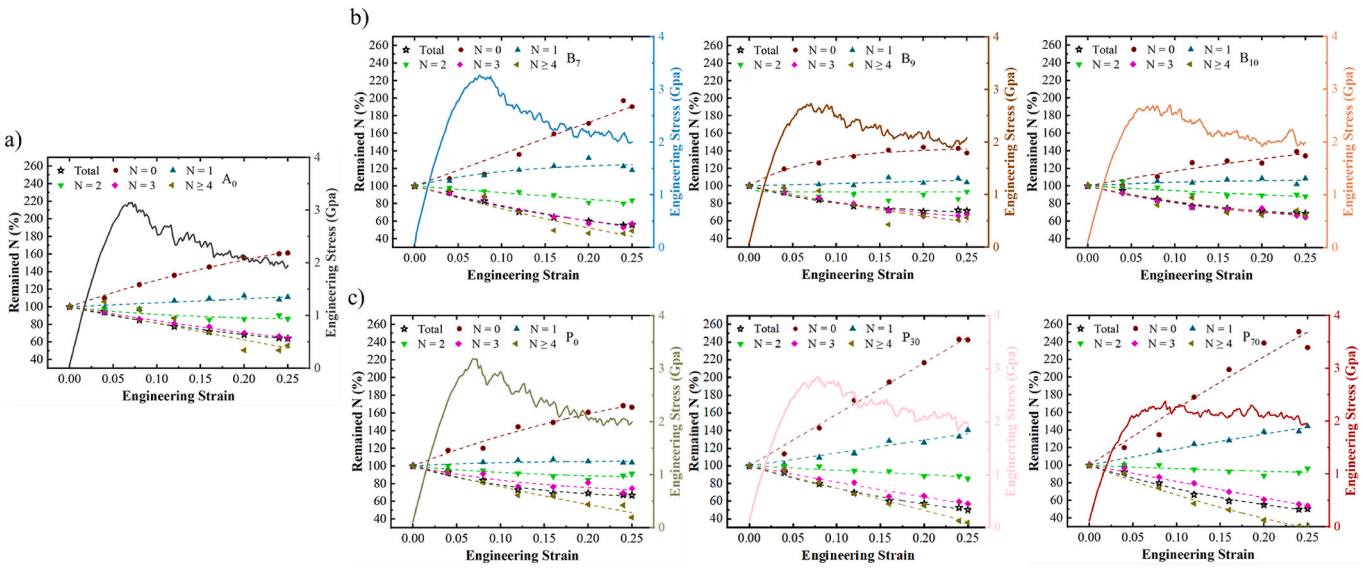

Fig. 8. Stress-strain curves and percentage change of ICOI with different N in a) A_0, the specimens under b) recovery annealing treatment and c) thermal-pressure treatment.

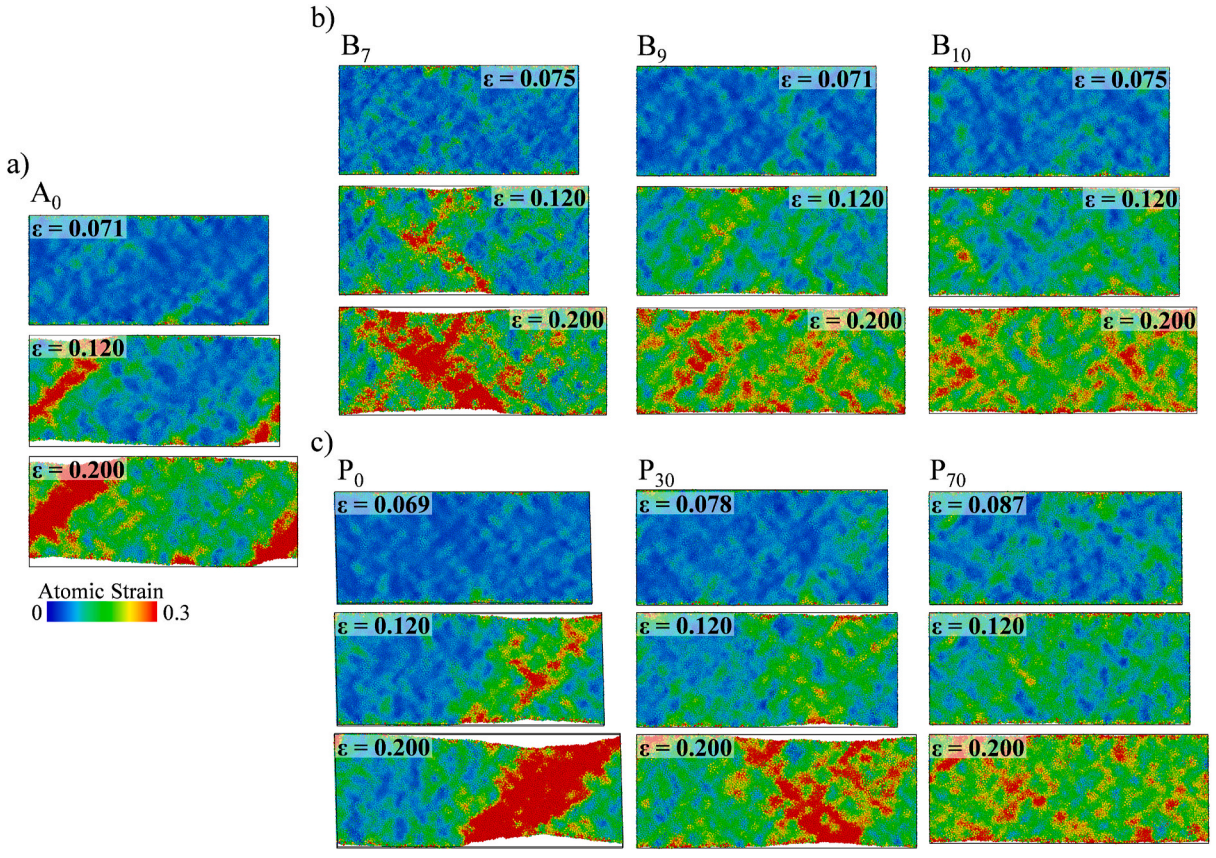

Fig. 9. Atomic shear strain diagram during the tensile process of a) A_0, the specimens under b) recovery annealing treatment and c) thermal pressure treatment.

exhibits notable similarities to that of A_0. Shear bands are formed after yielding and subsequently extend continuously until traversing the entire specimen. The shear offset is observable in both P_0 and A_0. Under applied pressure, the shear bands do not fully mature, and the extension of shear bands in other directions can be observed. In P_{70} specimen, STZs are initially activated in large quantities in regions characterized by sparse atomic arrangements during deformation. As STZs grow, they continually disrupt the surrounding ICOIN. Consequently, owing to the widespread activation of STZs, these rejuvenated specimens fail to form a primary shear band, leading to a relatively uniform deformation pattern. In the specimens under thermal-pressure treatment, despite the increased denseness of ICOIN, the rise in icosahedral potential energy coupled with increased free volume contributes to reduced stability of ICOIN. This makes ICOI more prone to destroying and transforming into other clusters during tension. Consequently, this leads to enhanced ductility, albeit at the expense of reduced strength. Similar observations

were reported in the research conducted by Kim et al. [45] and Wang et al. [52]. In their studies, the incorporation of trace elements, though it escalated the count of icosahedra, led to the emergence of unstable icosahedra that demonstrated an increased disruption rate during deformation, culminating in heightened ductility of the specimens.

According to the researches by Lee et al. [53] and Li et al. [54], it has been observed that diverse cluster structures in MGs experience persistent disruptions and reconfigurations throughout the deformation process. Fig. 10 depicts the N distribution at σ_{over} elucidating the disintegration and transformation dynamics of N during tension of various specimens. Fig. 10 clearly shows that at σ_{over}, the destruction rate gradually decreases with increasing N values, while the rate of transformation progressively escalates. As depicted in Fig. 10(a), for the specimens under recovery annealing, both A_0 and B_7 display similar trends for $N \geq 4$. The proportion of high-N ICOI is destroyed at around 20%, whereas those transforming surpasses 50%. Conversely, B_9 and B_{10} manifest a divergent pattern. Accompanying the continual elevation in potential energy inside the specimens, the percentage of high-N ICOI destroyed gradually increases from about 20% in aged specimens to roughly 40%. Simultaneously, the proportion of high-N transforming decreases from 50% to approximately 40%.

Fig. 10(b) reveals that for specimens under thermal-pressure treatment, a pattern akin to that in Fig. 10(a) emerged, characterized by an increased disruption rate of high-N and a decreased transformation rate after rejuvenation. During tension, a decreased proportion of high-N ICOI promotes the seamless expansion of activated STZs, thus augmenting the ductility. In summary, the distribution of N at σ_{over} potentially correlates with the strength and ductility characteristics of the specimens.

4. Conclusions

This study investigates the atomic structure and mechanical properties of $Cu_{64}Zr_{36}$ MG under recovery annealing and thermal-pressure treatments. We have drawn the main conclusions as follows.

(1) The common characteristic of the rejuvenated specimens under different rejuvenation methods is that an increase in the potential energy of the rejuvenated specimens correlated with enhanced ductility and reduced strength. During tension, the increased destruction rate and the reduced transformation rate of ICOIN in the rejuvenated specimens decrease atomic packing density. It offers increased potential sites for the activation and growth of STZs. The deformation mechanism of the rejuvenated specimens transitions from isolated shear band to homogeneous deformation, which significantly reduces the degree of deformation localization.

(2) The free volume, ICOIN density, and the evolution of ICOIN during tension exhibit converse characteristics in the specimens under different rejuvenation methods. In the rejuvenated specimens under recovery annealing, an increase in annealing temperature leads to a reduction in icosahedra, which results in increased free volume and decreased ICOIN density. In the specimens under thermal-pressure treatment, an increase in pressure leads to an increased number of icosahedra, which results in decreased free volume and increased ICOIN density. After tension, the rejuvenated specimens under high pressure have a significant reduction in ICOIN density compared to those under recovery annealing.

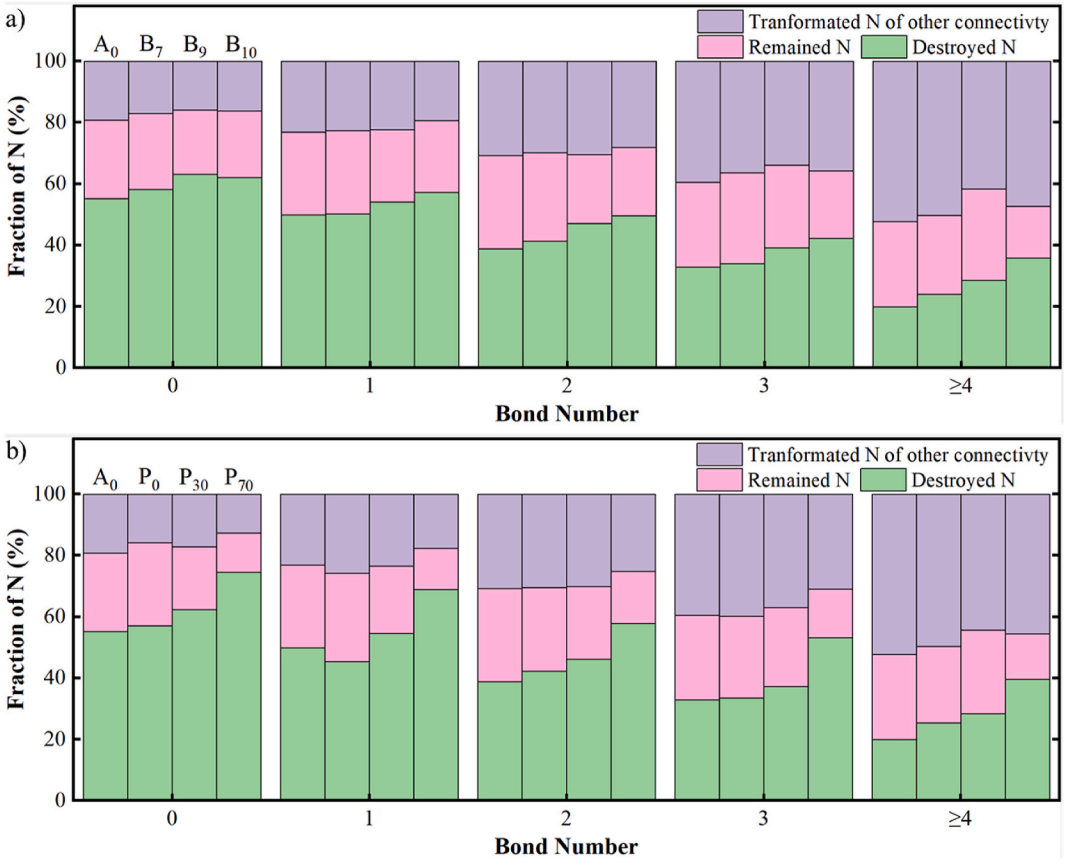

Fig. 10. Changes in ICOI with different N when the stress of the specimens is σ_{over} under a) recovery annealing treatment and b) thermal pressure treatment. In the tension process, the deformation and fracture of ICOIN cause ICOI with different N to be transformed or destroyed. This fraction is the ratio of the number of bonds when the specimen stress is σ_{over} to that before tension.

(3) Both the two rejuvenation methods improve the ductility of the specimens but in different ways. For the rejuvenated specimens treated by recovery annealing, the reduction in ICOIN density increases the number of the high σ_{Mises} regions, which increases the potential nucleation sites for STZs. More STZs are activated and uniformly distributed in the specimen, which inhibits the formation of isolated localized shear band. This leads to an increase in ductility of the rejuvenated specimens under recovery annealing. In contrast to the rejuvenated specimens under recovery annealing, the excessively increased icosahedral free volume of the specimens under high pressure reduces the stability of ICOIN. The activation and growth of STZs in the unstable ICOIN regions lead to an enhancement in ductility of the rejuvenated specimens under thermal-pressure treatment.

Declaration of competing interest

The authors declare that they have no known competing financial interests or personal relationships that could have appeared to influence the work reported in this paper.

Acknowledgments

The work was supported by the National Natural Science Foundation of China (No. 51601019, 52071089); Guangdong Major Project of Basic and Applied Basic Research (Grant No.2019B030302010); the Guangdong Basic and Applied Basic Research Foundation (NO. 2022A1515010233, 2024A1515010878).

Appendix A. Supplementary data

Supplementary data to this article can be found online at https://doi.org/10.1016/j.jmrt.2024.07.178.

References

[1] Chen K, Zhan L, Xu Y, Ma B, Zeng Q, Luo S. Optimizing strength and ductility in 7150 Al alloys via rapid electropulsing cyclic heat treatment. J Alloys Compd 2022;903:163985.
[2] Telford M. The case for bulk metallic glass,. Mater. Today 2004;7:36–43.
[3] Miracle DB. The efficient cluster packing model - an atomic structural model for metallic glasses. Acta Mater 2006;54:4317–36.
[4] Lee M, Lee CM, Lee KR, Ma E, Lee JC. Networked interpenetrating connections of icosahedra: effects on shear transformations in metallic glass. Acta Mater 2011;59:159–70.
[5] Feng SD, Chan KC, Zhao L, Pan SP, Qi L, Wang LM, Liu RP. Rejuvenation by weakening the medium range order in $Zr_{46}Cu_{46}Al_8$ metallic glass with pressure preloading: a molecular dynamics simulation study. Mater Des 2018;158:248–55.
[6] Ding J, Ma E, Asta M, Ritchie RO. Second-nearest-neighbor correlations from connection of atomic packing motifs in metallic glasses and liquids. Sci Rep 2015;5:17429.
[7] Wu ZW, Li FX, Huo CW, Li MZ, Wang WH, Liu KX. Critical scaling of icosahedral medium-range order in CuZr metallic glass-forming liquids. Sci Rep 2016;6:35967.
[8] Wu ZW, Wang WH. Linking local connectivity to atomic-scale relaxation dynamics in metallic glass-forming systems. Acta Phys Sin 2020;69:206–21.
[9] Wu ZW, Li MZ, Wang WH, Liu KX. Correlation between structural relaxation and connectivity of icosahedral clusters in CuZr metallic glass-forming liquids. Phys Rev B 2013;88:054202.
[10] Guo W, Shao Y, Zhao M, Lü S, Wu S. Varying the treating conditions to rejuvenate metallic glass by deep cryogenic cycling treatment. J Alloys Compd 2020;819:152997.
[11] Narasimhan R, Tandaiya P, Singh I, Narayan RL, Ramamurty U. Fracture in metallic glasses: mechanics and mechanisms. Int J Fract 2015;191:53–75.
[12] Haruyama O, Kisara K, Yamashita A, Kogure K, Yokoyama Y, Sugiyama K. Characterization of free volume in cold-rolled $Zr_{55}Cu_{30}Ni_5Al_{10}$ bulk metallic glasses. Acta Mater 2013;61:3224–32.
[13] Zhang Y, Wang WH, Greer AL. Making metallic glasses plastic by control of residual stress. Nat Mater 2006;5:857–60.
[14] Chu F, Han B, Edalati K, Ma J, Meng Y, Wang C, Yang F, Zhang P, Lin H-J. Severe plastic deformed Pd-based metallic glass for superior hydrogen evolution in both acidic and alkaline media. Scr. Mater. 2021;204:114145.
[15] Ketov SV, Sun YH, Nachum S, Lu Z, Checchi A, Beraldin AR, Bai HY, Wang WH, Louzguine-Luzgin DV, Carpenter MA, Greer AL. Rejuvenation of metallic glasses by non-affine thermal strain. Nature 2015;524:200–3.
[16] Sun K, Wang G, Wang YW, Chen HC, Yan L, Pauly S, Wu YH, Weber H, Wang Q, Huang B, Jia YD, Yi J, Zhai QJ. Structural rejuvenation and relaxation of a metallic glass induced by ion irradiation. Scr. Mater. 2020;180:34–9.
[17] Saida Jj, Yamada R, Wakeda M. Recovery of less relaxed state in Zr-Al-Ni-Cu bulk metallic glass annealed above glass transition temperature. Appl Phys Lett 2013;103:221910.
[18] Wang C, Yang ZZ, Ma T, Sun YT, Yin YY, Gong Y, Gu L, Wen P, Zhu PW, Long YW, Yu XH, Jin CQ, Wang WH, Bai HY. High stored energy of metallic glasses induced by high pressure. Appl Phys Lett 2017;110:111901.
[19] Wang MZ, Lü SL, Wu SS, Chen XH, Guo W. Rejuvenation behaviors of recovery-annealed Cu-Zr metallic glass with different thermal treatment conditions: a molecular dynamics study. J Mater Res Technol 2022;20:3355–62.
[20] Wang MZ, Lü SL, Wu SS, Guo W. Rejuvenation behavior and microstructural evolution of Cu-Zr metallic glass during multiple recovery annealing treatment via molecular dynamic simulation. J Alloys Compd 2023;945:169294.
[21] Amigo N, Valencia F. Mechanical and structural assessment of CuZr metallic glasses rejuvenated by thermal-pressure treatments. Comput Mater Sci 2021;198:110681.
[22] Amigo N, Valencia FJ. Species content effect on the rejuvenation degree of CuZr metallic glasses under thermal-pressure treatments. Met Mater Int 2022;28:2068–74.
[23] Thompson AP, Aktulga HM, Berger R, Bolintineanu DS, Brown WM, Crozier PS, in 't Veld PJ, Kohlmeyer A, Moore SG, Nguyen TD, Shan R, Stevens MJ, Tranchida J, Trott C, Plimpton SJ. Lammps - a flexible simulation tool for particle-based materials modeling at the atomic, meso, and continuum scales. Comput Phys Commun 2022;271:108171.
[24] Mendelev MI, Kramer MJ, Ott RT, Sordelet DJ, Yagodin D, Popel P. Development of suitable interatomic potentials for simulation of liquid and amorphous Cu-Zr alloys. Philos Mag 2009;89:967–87.
[25] Mattern N, Schöps A, Kühn U, Acker J, Khvostikova O, Eckert J. Structural behavior of CuxZr100−x metallic glass (x=35−70). J Non-Cryst Solids 2008;354:1054–60.
[26] Saida J, Yamada R, Wakeda M, Ogata S. Thermal rejuvenation in metallic glasses. Sci Technol Adv Mater 2017;18:152–62.
[27] Li S, Zhang JC, Sha ZD. Mechanical behavior of metallic glasses with pressure-promoted thermal rejuvenation. J Alloys Compd 2020;848:156597.
[28] Nosé S. A unified formulation of the constant temperature molecular dynamics methods. J Chem Phys 1984;81:511–9.
[29] Parrinello M, Rahman A. Polymorphic transitions in single crystals: a new molecular dynamics method. J Appl Phys 1981;52:7182–90.
[30] Cao AJ, Cheng YQ, Ma E. Structural processes that initiate shear localization in metallic glass. Acta Mater 2009;57:5146–55.
[31] Feng SD, Li L, Chan KC, Zhao L, Wang LM, Liu RP. Enhancing strength and plasticity by pre-introduced indent-notches in $Zr_{36}Cu_{64}$ metallic glass: a molecular dynamics simulation study. J Mater Res Technol 2020;43:119–25.
[32] Stukowski A. Visualization and analysis of atomistic simulation data with OVITO-the open visualization tool. Model. Simul. Mat. Sci. Eng. 2010;18:015012.
[33] Yuan X, Şopu D, Spieckermann F, Song KK, Ketov SV, Prashanth KG, Eckert J. Maximizing the degree of rejuvenation in metallic glasses. Scr. Mater. 2022;212:114575.
[34] Wang MZ, Liu HS, Li JY, Jiang Q, Yang WM, Tang CG. Thermal-pressure treatment for tuning the atomic structure of metallic glass Cu-Zr. J Non-Cryst Solids 2020;535:119963.
[35] Miracle DB. A structural model for metallic glasses. Nat Mater 2004;3:697–702.
[36] Medvedev NN. The algorithm for three-dimensional voronoi polyhedra. J Comput Phys 1986;67:223–9.
[37] Li MZ, Peng HL, Hu YC, Li FX, Zhang HP, Wang WH. Five-fold local symmetry in metallic liquids and glasses. Chin Phys B 2017;26:016104.
[38] Amigo N. Role of high pressure treatments on the atomic structure of cuzr metallic glasses. J Non-Cryst Solids 2022;576:121262.
[39] Miyazaki N, Lo Y-C, Wakeda M, Ogata S. Properties of high-density, well-ordered, and high-energy metallic glass phase designed by pressurized quenching. Appl Phys Lett 2016;109.
[40] Yang MH, Li JH, Liu BX. Proposed correlation of structure network inherited from producing techniques and deformation behavior for Ni-Ti-Mo metallic glasses via atomistic simulations. Sci Rep 2016;6:29722.
[41] Wakeda M, Saida J, Li J, Ogata S. Controlled rejuvenation of amorphous metals with thermal processing. Sci Rep 2015;5:10545.
[42] Miyazaki N, Wakeda M, Wang Y-J, Ogata S. Prediction of pressure-promoted thermal rejuvenation in metallic glasses. npj Comput Mater 2016;2:16013.
[43] Zhang J, Wang X, Li M. From brittle to ductile transition: the influence of oxygen on mechanical properties of metallic glasses. J Alloys Compd 2021;876:160023.
[44] Guo QW, Hou H, Wang KL, Li MX, Liaw PK, Zhao YH. Coalescence of $Al_{0.3}$CoCrFeNi polycrystalline high-entropy alloy in hot-pressed sintering: a molecular dynamics and phase-field study. npj Comput Mater 2023;9:1–13.
[45] Kim HK, Lee M, Lee KR, Lee JC. How can a minor element added to a binary amorphous alloy simultaneously improve the plasticity and glass-forming ability? Acta Mater 2013;61:6597–608.
[46] Peng CX, Şopu D, Cheng Y, Song KK, Wang SH, Eckert J, Wang L. Deformation behavior of designed dual-phase CuZr metallic glasses. Mater Des 2019;168:107662.
[47] Şopu D, Moitzi F, Mousseau N, Eckert J. An atomic-level perspective of shear band formation and interaction in monolithic metallic glasses. Appl Mater Today 2020;21:100828.
[48] Zhou H, Shen L, Sun B, Wang W. Research progress on the shear band of metallic glasses. J Alloys Compd 2023;955:170164.

[49] Yuan X, Şopu D, Moitzi F, Song KK, Eckert J. Intrinsic and extrinsic effects on the brittle-to-ductile transition in metallic glasses. J Appl Phys 2020;128:125102.
[50] Wang Q, Li JH, Liu JB, Liu BX. Structural skeleton of preferentially interpenetrated clusters and correlation with shear localization in Mg-Cu-Ni ternary metallic glasses. Phys Chem Chem Phys 2014;16:19590–601.
[51] Foroughi A, Tavakoli R, Aashuri H. Medium range order evolution in pressurized sub-Tg annealing of $Cu_{64}Zr_{36}$ metallic glass. J Non-Cryst Solids 2018;481:132–7.
[52] Wang PF, Peng CX, Cheng Y, Jia LJ, Wang YY, Wang L. Atomic structure evolution of $(CuZr)_{100-x}Ag_x$ glass under compression deformation. J Alloys Compd 2019;777:44–51.
[53] Lee CM, Park KW, Lee BJ, Shibutani Y, Lee JC. Structural disordering of amorphous alloys: a molecular dynamics analysis. Scr. Mater. 2009;61:911–4.
[54] Li CL, Wei YJ, Shi XH. Reformation capability of short-range order and their medium-range connections regulates deformability of bulk metallic glasses. Sci Rep 2015;5:12177.